https://doi.org/10.5194/egusphere-2024-860
Preprint. Discussion started: 11 April 2024

Elucidating the boundary layer turbulence dissipation rate using high-resolution measurements from a radar wind profiler network over the Tibetan Plateau

Deli Meng[1], Jianping Guo[1,2*] Xiaoran Guo[1], Yinjun Wang[1], Ning Li[1], Yuping Sun[1], Zhen Zhang[1], Na Tang[1], Haoran Li[1], Fan Zhang[1], Bing Tong[3], Hui Xu[1], Tianmeng Chen[1]

[1]State Key Laboratory of Severe Weather, Chinese Academy of Meteorological Sciences, Beijing 100081, China

[2]Fujian Key Laboratory of Severe Weather, Fujian Institute of Meteorological Sciences, Fuzhou 350028, China

[3]State Key Laboratory of Urban and Regional Ecology, Research Center for Eco-Environmental Sciences, Chinese Academy of Sciences, Beijing 100085, China

Correspondence to: Dr/ Prof. Jianping Guo (Email: jpguocams@gmail.com)

https://doi.org/10.5194/egusphere-2024-860
Preprint. Discussion started: 11 April 2024

Abstract

The planetary boundary layer (PBL) over the Tibetan Plateau (TP) exerts a significant influence on regional and global climate, while its vertical structures of turbulence and evolution features remain poorly understood, largely due to the scarcity of observation. This study examines the vertical profile and daytime variation of turbulence dissipation rate (ε) in the PBL over the TP using the high-resolution (6 min and 120 m) measurements from the radar wind profiler (RWP) network, combined with the hourly data from the ERA5 reanalysis. Observational analyses show that the magnitude of ε below 3km under all-sky conditions exhibits large spatial discrepancy over the six RWP sites over the TP. Particularly, the values of ε at Minfeng and Jiuquan over the northern TP and Dingri over the southern TP are roughly an order of magnitude greater than those at Lijiang, Ganzi and Hongyuan over the eastern TP. This could be partially attributed to the difference of land cover across the six RWP sites. In terms of the diurnal variation, ε rapidly intensifies from 0900 local standard time (LST) to 1400 LST, and then gradually levels off in the late afternoon. Under clear-sky conditions, both ε and planetary boundary layer height (z_i) are greater, compared with cloudy-sky conditions. This reveals that clouds would suppress the turbulence development and deduce z_i. In the lower PBL (0.2<z/z_i<0.5, where z is the height above ground level), the dominant influential factor for the development of turbulence is the surface-air temperature difference ($T_s - T_a$). By comparison, in the upper PBL (0.6<z/z_i<1.0), both the $T_s - T_a$ and vertical wind shear (VWS) affect the development of turbulence. Above the PBL (1.0<z/z_i<2.0), the shear production resulting from VWS dominates the variation of turbulence. Under cloudy-sky conditions, clouds are found to decrease the surface total solar radiation, thereby reducing $T_s - T_a$ and surface sensible heat flux. This weakened sensible heat flux tends to inhibit the turbulent motion within PBL especially in the lower PBL and decrease the growth rate of z_i. On the other hand, the strong VWS induced by clouds enhances the turbulence above the PBL. The findings obtained here underscore the importance of RWP network in revealing the fine-scale structures of the PBL over the TP and gaining new insight into the PBL evolution.

https://doi.org/10.5194/egusphere-2024-860
Preprint. Discussion started: 11 April 2024

1. Introduction

Turbulence ranks among the most intricate phenomena within the atmosphere, ensuring that the planetary boundary layer (PBL) remains thoroughly mixed during daylight hours (Li et al., 2023). As a result, the structure of the PBL is, to a considerable extent, governed by the evolution of turbulence (Teixeira et al., 2021). Turbulence dissipation rate (ε) reflects the amount of turbulent kinetic energy (TKE) that is converted into heat at the Kolmogorov scale and is a measure of the turbulence intensity (McCaffrey et al., 2017; Muñoz-Esparza et al., 2018). Proper parameterizations of the turbulence dissipation term with the aid of observations have great impact on the model forecast skill for the weather and climate, as ε strongly affects vertical turbulent mixing through its influence on TKE (Yang et al., 2017). Accurate estimation of ε is crucial for understanding the structure of turbulence in the PBL. To date, a variety of instruments have been used to observe or retrieve the vertical profiles of ε, including sodar, radar wind profiler (RWP), radiosonde, Doppler wind lidar (DWL) and ultrasonic anemometer (Dodson and Griswold, 2021; Jacoby-Koaly et al., 2002; Kotthaus et al., 2023; Lv et al., 2021). Compared with the DWL, the RWP exhibit better capability in capturing the turbulence structures in the cloudy sky. Furthermore, it is hard for the radiosonde and ultrasonic anemometer to get the temporal continuous measurements of the atmospheric turbulence, due to the high costs.

The Tibetan Plateau (TP), with an averaged elevation above 4000 m and an area of approximately 2.5 million km^2, is towering into the lower and middle troposphere (Huang et al., 2023). By receiving a greater amount of solar shortwave radiation, the surface layer of the TP could transfer more heat through the PBL to the free atmosphere (Ma et al., 2023; Wang et al., 2015). The PBL over the TP exhibits strong convective bubbling and upward motions due to the lower air density and buoyancy effect, which results in significant turbulence motions and turbulence-convection interactions with "popcorn" cloud structures (Xu et al., 2002; Xu et al., 2023). Understand the statistical behavior of ε is key to revealing the vertical structure and evolution of PBL turbulence, which could improve the parameterization of PBL processes over the TP (Ma et al., 2023; Wang et al., 2015; Xu et al., 2019; Zhao et al., 2019). However, due to the limited observations of turbulence

https://doi.org/10.5194/egusphere-2024-860
Preprint. Discussion started: 11 April 2024

profiles, the daytime variation characteristics of ε over the TP and its main influential mechanisms remains poorly understood.

A vast range of previous studies have attempted to figure out the mechanisms behind the observed turbulence, but most of them are based on radiosonde measurements or model simulation or reanalysis data (e.g., Banerjee et al., 2018; Che and Zhao, 2021; Wang et al., 2023a). A myriad of driving mechanisms is proposed to account for the PBL development over the TP, such as surface thermal and dynamic forcing, atmosphere stability, among others (Chechin et al., 2023; Chen et al., 2016; Lai et al., 2021; Wang et al., 2023a; Wang and Zhang, 2022). It has been demonstrated that the buoyancy term contribution on the southern slope of the TP is significantly larger than that on the southeastern edge of the TP (Wang et al., 2015). A larger surface-air temperature difference ($T_s - T_a$) and sensible heat flux could promote the rapid growth of deep PBL in the western and southern TP (Chen et al., 2013, 2016; Li et al., 2017a; Wang et al., 2016; Zhang et al., 2022). Chen et al (2016) found that the weak atmosphere stability at the top of the mixed layer is a key factor contributing to the rapid growth of the deep turbulence in winter over the TP.

Also, cloud radiative effects are found to be another significant factor to modulate the evolution of daytime PBL turbulence (Bodenschatz et., 2010). The TP is characterized by a high frequency of cumulus clouds which is about five times the regional mean over the other areas of China (Wang et al., 2015), and the occurrence frequency of clouds over the TP shows large diurnal and spatial variability, with the maxima in the afternoon in the eastern TP (Wan et al., 2022). Guo et al. (2019) has revealed that the cloud tends to suppress the development of summer PBL in the early afternoon across China using the fine-resolution radiosonde observations. Under continuous cloudy-sky conditions, the convective PBL develops slowly due to the smaller surface sensible heat compared to the clear-sky conditions (Wang and Zhang, 2022). The turbulence motion and dynamic structure in the PBL is contributed to the formation and development of the popcorn-like convective clouds (Wang et al., 2020; Xu et al., 2002). Based on surface observation, radiosonde, satellite and reanalysis data, Wang et al. (2020) pointed out that higher PBL height and lower lifting condensation level due to lower temperature and lower atmospheric density may enhance low cloud occurrence in the afternoon, and in turn influencing PBL development over the TP. However, the turbulence structure differences between clear-sky

https://doi.org/10.5194/egusphere-2024-860
Preprint. Discussion started: 11 April 2024

and cloudy-sky conditions are rarely explored, and the possible mechanism influencing the cloud topped PBL turbulence evolution remains elusive. To the best of our knowledge, most of the above-mentioned studies over the TP lack high-temporal resolution turbulence profile observations. Coincidently, there exists a RWP network of China, which provides us an invaluable opportunity to characterize the PBL turbulence structure over the TP (Guo et al., 2021a). Therefore, the main objective of this study is to resolve the above issues over the TP, by using observations from the RWP network together with other ground-based meteorological measurements and the ERA5 data. We also analyze the joint effect of thermodynamic and dynamic on ε structure in the daytime (0900–1700 LST) PBL through $T_s - T_a$ and vertical wind shear (VWS).

The remainder of this manuscript proceeds as follows, Section 2 describes the data and methods used in this study. In Section 3, we analyze the spatio-temporal characteristics and daytime pattern of ε over the TP and investigate the possible thermodynamic and dynamic effect on PBL turbulence under clear-sky and cloudy-sky conditions. The summary and conclusions are given in section 4.

2. Data and methods

2.1 The RWP network over the TP

In this study, we use the vertical measurements of RWP data with a vertical resolution of 120 m and a temporal resolution of 6-min from the RWP network over the TP, which contains six operational sites (Minfeng, Jiuquan, Hongyuan, Ganzi, Lijang and Dingri) operated by the China Meteorological Administration (CMA) during the period from September 1, 2022 to November 31, 2023. The spatial distribution of RWP network over the TP is shown in Fig. 1, and the detailed information for each RWP site, including longitude, latitude, elevation, and land cover type is given in Table 1. Among these six RWP sites, the Dingri site is located in the foothills of the Himalayas with an elevation more than 4,300m above sea level (AGL), dominated by the land cover of bare and alpine grassland. The Lijiang site is located in the southeastern TP characterized by complex

https://doi.org/10.5194/egusphere-2024-860
Preprint. Discussion started: 11 April 2024

terrain with an elevation of about 2,400m AGL. The Ganzi and Hongyuan sites are situated in the eastern TP, with elevations ranging from 3,300 to 3,500m AGL, and whose underlay is mainly alpine grassland. The Minfen and Dunhuang sites are situated in arid and semi-arid zones to the north of the TP, with elevations ranging from 1,400 to 1,500m, and their dominant underlying land cover is mainly bare land. Therefore, these two sites are well representative of the northern TP.

The RWP has the capability to obtain the high-temporal resolution atmospheric turbulence and wind profiles over the TP compared to the radiosonde and reanalysis, which makes it possible to analyze the fine PBL structures. The low and medium detection modes of RWPs can acquire the wind field and turbulence information bellow 5 km AGL (McCaffrey et al., 2017; Ruan et al., 2014). The RWP provides the radial observations (marked as RAD subset), including profiles of radial velocity, doppler spectral width, and signal noise ratio. Also provided by the RWP is the real-time sampling data (marked as ROBS subset), including the profiles of horizontal wind (direction and speed), vertical velocity, and refractive index structure constant (Liu et al., 2020). There exist large uncertainties in the profiling measurements from RWP, thus the quality control for both RAD and ROBS subsets are indispensable before retrieving related dynamic variables over the TP (Liu et al., 2020; Wang et al., 2023). For instance, the profiling measurements highly deviate from the truth below 0.5 km AGL and above 5 km AGL, which are attributed to the near-surface clutter and significant beam attenuation, respectively (Guo et al., 2023). Thus, here only the RWP measurements at heights from 0.5 km to 5 km are utilized for analysis.

2.2 Other miscellaneous meteorological data

In this study, the hourly ground-based meteorological variables, including 2m air temperature (T_a), ground surface temperature (T_s), pressure and cloud cover, are derived from the six automatic weather sites over the TP. Also, 1-min rainfall observations from rain gauges are used to minimize the potential influence of rainfall on the profiling measurements from RWP. All these meteorological datasets are subjected to strict data-quality control by the National Meteorological Information Center (NMIC) of the China

https://doi.org/10.5194/egusphere-2024-860
Preprint. Discussion started: 11 April 2024

Meteorological Administration (Wang et al., 2023b). In addition, the hourly temperature data at pressure levels from the ERA5 reanalysis data is also used in this study (Hersbach et al., 2020).

2.3 Methods

2.3.1 Retrieval of turbulence dissipation rate

As a widely used ground-based equipment for detecting atmospheric wind profile (Liu et al., 2020), RWP has the advantage to estimate ε since it could measure Doppler velocity spectrum in the radar volume where the turbulence parcel motion accounts for the spectral width broadening (Jacoby-Koaly et al., 2002; White, 1999). In this study, the spectral width method is applied to retrieve ε from the RAD subset based on the hypothesis that turbulence is isotropic, and the contributions to the spectral width from turbulent and non-turbulent process are independent of each other (Solanki et al., 2021; White, 1999).

The major steps for ε retrieval can be summarized as follows: (1) the spectral width variance consisting of the turbulence and non-turbulence variance is obtained from the spectral width measurements. (2) The non-turbulence broadening variances are decomposed into beam broadening variance due to the finite width of the beam, shear broadening variance generated by the presence of a wind gradient, and broadening variance arising from data processing, among others (Nastrom, 1997). (3) The turbulent broadening variance is extracted from the spectral width variance by excluding above mentioned non-turbulence broadening variances. (4) ε is estimated from turbulent broadening variance with the main assumption of isotropic and homogeneous turbulence, as well as Gaussian antenna symmetric illumination function and Gaussian radial response of the receiver (White et al., 1999). For more details for the spectral width method, refer to the references (Jacoby-Koaly et al., 2002; McCaffrey et al., 2017; Nastrom, 1997; Solanki et al., 2021).

2.3.2 Estimation of planetary boundary layer height

The planetary boundary layer height (hereafter referred to as z_i) is an important parameter for characterizing fine vertical structure of the PBL, which has important implications for the air mass exchange between Earth's surface and the atmosphere aloft,

https://doi.org/10.5194/egusphere-2024-860
Preprint. Discussion started: 11 April 2024

thus affecting the cloud development and air pollutant dispersion (Dai et al., 2014; Dodson and Griswold, 2021; Guo et al., 2021a; Li et al., 2017b; Wang et al., 2022).

Here daytime z_i at each RWP site is derived from original signal-to-noise ratio (SNR) profiles from the RAD subset based on the improved threshold method (ITM). The steps are briefly outlined as follows. First of all, here we use the profile of normalized SNR (NSNR) to avoid instrumental inconsistencies. Secondly, the NSNR threshold is set to 0.75 based on the z_i estimated by the radiosonde measurements at the same site. Thirdly, the profile of NSNR is scanned downwardly from the top to the ground surface. Finally, z_i ultimately is determined as the height where the NSNR profile greater than 0.75 for the first time. For more details for the ITM, refer to the references (Liu et al., 2019).

2.3.3 Vertical wind shear

The ROBS subset is used to calculate vertical wind shear (VWS), which is an important parameter that present the dynamical effect on the development of PBL (Zhang et al., 2020). VWS can be calculated as follows.

$$\mathrm{VWS} = \left[\left(\frac{\partial u}{\partial z}\right)^2 + \left(\frac{\partial v}{\partial z}\right)^2\right]^{1/2} \tag{1}$$

where u and v denote zonal and meridional wind component, respectively, z denotes the sample height AGL.

2.3.4 Classification of cloudy- and clear-sky conditions

Using RWP combined with the ground-based cloud cover observations at each site, the effect of clouds on daytime variations of PBL turbulence and z_i over the TP are investigated. Firstly, the 1-min precipitation and 6-min RWP data are time-matched to remove the profile data half an hour before and after the precipitation to obtain non-precipitation data (Wu et al, 2023). Then, all-sky conditions are defined as non-precipitation hours. Finally, the clear-sky (cloudy-sky) conditions are identified as hours with the cloud fraction less (greater) than 30% (80%), respectively (Guo et al., 2016; Solanki et al., 2021).

https://doi.org/10.5194/egusphere-2024-860
Preprint. Discussion started: 11 April 2024

2.3.5 Calculation of the gradient Richardson number

The evolution of turbulence in the PBL has been previously recognized to be closely associated with atmospheric stability (Chechin et al., 2023; Chen et al, 2013; Lai et al., 2021; Muhsin et al., 2016). Therefore, we take the gradient Richardson number (Ri) as a variable to characterize atmospheric stability and the formation of turbulence over the TP. Following Stull (1988), Ri is formulated as follows:

$$Ri = \frac{g}{\theta_v} \frac{\partial\theta_v/\partial z}{(\partial u/\partial z)^2 + (\partial v/\partial z)^2} \quad (2)$$

where θ_v is the virtual potential temperature from ERA5, u and v are the hourly zonal and meridional wind components derived from RWP, respectively, g is the gravitational acceleration, and z represents the AGL.

3. Results and discussion

3.1 Spatio-temporal distributions of daytime PBL turbulence dissipation rate

Both the PBL turbulence dissipation rate and z_i have significant diurnal variations over mountain and urban areas (Adler et al., 2014; Liu et al., 2019; Solanki et al., 2021; Yang et al., 2023). Since the longitude of the six sites over the TP is ranged from 82.7°E to 102.6°E, it is necessary to use the Local Standard Time (LST) to accurately capture the daytime variations of the PBL and make a comparison between different sites.

Figure 2 presents a comprehensive overview of the ε profile at 6 min intervals and hourly averaged z_i in lower troposphere at heights from 0.5 km to 3.0 km for six RWP sites over the TP during the period from September 1, 2022 to November 31, 2023. The magnitude of ε and its vertical structures during the daytime at both Minfeng and Jiuquan sites over the northern TP and at Dingri site over the southern TP stand in stark contrast to those RWP sites (i.e., Lijiang, Ganzi and Hongyuan) in the eastern TP. As shown in the right panels of Fig. 2, ε generally decrease with increased height at all six RWP sites. It is apparent that ε exhibits a larger west-east and north-southern spatial difference under all-sky conditions. In terms of the latitudinal variation, ε exhibits a decreasing trend from west

https://doi.org/10.5194/egusphere-2024-860
Preprint. Discussion started: 11 April 2024

to east at both Minfeng and Jiuquan sites along the altitude belt of 38°N, so does the RWP sites of Dingri, Lijiang, Ganzi and Hongyuan along the altitude belt of 30°N. In terms of the meridional variation, ε at the two RWP sites in the northern TP have a significantly larger magnitude than the other four sites. In particularly, the maximum mean value of daytime ε in the height range of 0.5 to 3.0 km is found at Minfeng and Jiuquan in the northern TP, which reaches up to $10^{-3.59}$ m^2 s^{-3} and $10^{-3.73}$ m^2 s^{-3}, respectively. By comparison, the least magnitude of ε is found in the eastern TP, with the mean values of $10^{-4.06}$ m^2 s^{-3}, $10^{-4.30}$ m^2 s^{-3} and $10^{-4.22}$ m^2 s^{-3} at Lijiang, Hongyuan and Ganzi, respectively. Meanwhile, the mean magnitude of ε at Dingri in the southern TP lies between the magnitude of ε in the northern and eastern TP, which is $10^{-3.88}$ m^2 s^{-3}.

The above results imply that the turbulence intensity at the RWP sites over the northern and western TP is about one order of magnitude greater than that in the eastern TP. To further investigate the possible reasons for this significant difference in ε, the relationships between $T_s - T_a$ and ε for different regions are presented in Fig. 3. The mean value of $T_s - T_a$ in the northern and southern TP is 14.29°C, which is greater than that of eastern TP with the value of 11.26°C (Fig. 3a). The mean daytime ε for the two regions reaches up to $10^{-3.74}$ m^2 s^{-3} and $10^{-4.20}$ m^2 s^{-3}, respectively (Fig. 3b). Additionally, ε is significantly and positively correlated with $T_s - T_a$ (R>0.35, p<0.005), which illustrates that the thermal forcing makes an important contribution to turbulence development in the TP (Figs. 3c and 3d).

Overall, the spatial distribution of the z_i at all six RWP sites is clearly dependent on geographical location (Fig. 2), which resembles that of the ε. The geographic pattern of z_i from RWP agrees well with those from radiosonde measurements (Che and Zhao, 2021) and reanalysis (Slättberg, 2022). The land surfaces at both Minfeng and Jiuquan sites in the northern TP are dominated by barren and relatively homogenous terrain, in sharp contrast to the highly vegetated underlying terrain at both Ganzi and Hongyuan sites in the eastern TP (Fig. 1). The sparse vegetation in the northern TP generally comes with large Bowen ratio during the daytime, which tends to produce larger sensible heat flux compared to that in the eastern TP. The increased turbulence intensity in PBL is generally associated with larger sensible heat flux, which has been reported by previous studies (Wang et al.,

https://doi.org/10.5194/egusphere-2024-860
Preprint. Discussion started: 11 April 2024

2016; Zhang et al., 2022). Thus, the spatial and magnitude of ε over the TP are most likely relevant to the underlying surface type.

Regarding the daytime pattern of turbulence (all six panels with color shading in Fig. 2), the turbulence over the TP shows a pronounced signature of single–peak variability. During the period 0900–1100 LST, the magnitude of ε at all six RWP sites is relatively weak. From 1100 LST onward, with the increase of downward solar shortwave radiation, surface sensible heat flux gradually rises, which leads to acceleration of turbulence mixing processes. Then, ε reaches peak in the early afternoon (1300–1500 LST). Afterwards, during the later afternoon (1500–1700 LST), ε diminishes gradually. Likewise, z_i almost follows the same daytime variation pattern of ε.

3.2 Characteristics of daytime PBL turbulence dissipation rate under clear- and cloudy-sky conditions

The influence of clouds on PBL has been discussed and analyzed in previous studies (e.g., Guo et al., 2016; Huang et al., 2023; Ma et al., 2023; Schumann et al., 1991; Yu et al., 2004). To reveal the potential impact of clouds on PBL ε over the TP, the comparison analyses between clear- and cloudy-sky conditions are presented in this section. Figure 4 shows the daytime cycle of mean ε profile and z_i averaged over the six RWP sites under all-, clear- and cloudy-sky conditions. Overall, both the profile of ε and z_i over the TP present distinct single–peak variations, and their peaks approximately occur at 1400 LST (Fig. 4a). The daytime averaged ε below 3.0 km AGL is $10^{-3.95}$ m^2 s^{-3}, and mean z_i is 1472 m, respectively. There is a significant positive correlation between ε and z_i during the daytime (R=0.63, p<0.01).

Under clear-sky condition, the daytime mean ε is $10^{-3.88}$ m^2 s^{-3} (Fig. 4b). During the period 1300–1500 LST, ε is ranged from $10^{-3.43}$ to $10^{-2.82}$ m^2 s^{-3} ($10^{-4.17}$ to $10^{-3.40}$ m^2 s^{-3}) at heights from 0.5 km (1.0 km) to 1.0 km (2.0 km) in lower (upper) PBL. Thus, the well-mixed turbulence maintains the development of PBL in the early afternoon. Under cloudy-sky condition (Fig. 4c), the daytime mean value of z_i can reach up to 1415 m, which is 117 m lower than that of clear-sky conditions. This means that the clouds would suppress

https://doi.org/10.5194/egusphere-2024-860
Preprint. Discussion started: 11 April 2024

the development of the PBL turbulence in the early afternoon which has been observed by the radiosonde observations described in Guo et al (2016).

Furthermore, the probability density distribution (PDF) of ε in PBL (0.2<z/z_i<1.0) and above the PBL (1.0<z/z_i<2.0) under all-, clear- and cloudy-conditions are given in Fig. 5. Here AGL (z) is normalized by z_i to provide a nondimensional vertical coordinate of z/z_i. Overall, the mean ε are $10^{-3.82}$, $10^{-3.79}$ and $10^{-3.85}$ m^2 s^{-3} at height of 0.2<z/z_i<2.0 under all-, clear- and cloudy-sky conditions, respectively (Fig. 5a). Within the PBL (Fig. 5b), the mean ε under clear-sky conditions ($10^{-3.27}$ m^2 s^{-3}) is greater than that of under cloudy-sky conditions ($10^{-3.36}$ m^2 s^{-3}), and the standard deviation of ε under clear-sky conditions is slightly greater than that under cloudy-sky conditions. This illustrates that clouds can significantly inhibit the turbulence intensity in the PBL, with the value of $\Delta\varepsilon$ between clear- and cloudy-sky conditions is -$10^{-4.0}$ m^2 s^{-3}. However, above the PBL (Fig. 5c), ε presents normal distribution characteristics, and there is no significant difference between the mean ε under clear- and cloudy-sky conditions.

To examine the impact of clouds on the vertical structure of turbulence within and above the PBL, Figure 5d shows the normalized contoured frequency by altitude diagram (NCFAD) of the $\Delta\varepsilon$ for normalized (z/z_i) profiles of ε between cloudy-sky and clear-sky conditions. Within the PBL, $\Delta\varepsilon$ is negative, and $|\Delta\varepsilon|$ generally decrease with increased z/z_i, where $\Delta\varepsilon$ is -$10^{-4.3}$ m^2 s^{-3} at z/z_i=0.5, and -$10^{-5.0}$ m^2 s^{-3} at z/z_i=1.0, respectively. This suggests that clouds may weaken turbulence within the PBL (Figs. 4b and 4c), especially in the lower PBL (z=820m, z/z_i<0.5).

3.3. Potential factors Influencing daytime PBL turbulence dissipation rate

3.3.1 Surface-air temperature difference

The vertical structure of PBL ε and z_i over the TP show obvious spatial differences in the context of a complex subsurface. The diverse land cover types lead to differences in surface albedo and soil moisture, which in turn lead to distinctions in thermodynamic characteristics such as sensible heat flux (Ma et al., 2023). Buoyant production driven by solar heating from the surface is one of the dominant sources generating turbulence in the

https://doi.org/10.5194/egusphere-2024-860
Preprint. Discussion started: 11 April 2024

convective PBL. The surface sensible heat flux is an important thermodynamic factor that affects the buoyant convective processes (Stull, 1988). Meanwhile, previous studies (e.g., Wang et al., 2022; Yang et al., 2023) have suggested that $T_s - T_a$ can serve as a good proxy for the sensible heat flux. There are not sensible heat flux measurements at six RWP sites in this study, and thus we directly take $T_s - T_a$ as a proxy thermodynamic variable to analyze its potential connection to variation of PBL turbulence.

Figure 6 shows the magnitude of ε varies as a function of $T_s - T_a$ for all six sites, within (0.2<z/z_i<1.0) and above (1.0<z/z_i<2.0) the PBL, under all, clear- and cloudy-sky conditions, respectively. $T_s - T_a$ are first classified into five bins, which are then statistically analyzed against the corresponding ε averaged for z/z_i values between 0.2 and 2.0 to obtain regression equations incorporating slopes. Further, Table 2 shows the scatter plots between $Log_{10}\varepsilon$ and $T_s - T_a$ (and VWS) at different altitude ranges under all-, clear- and cloudy-sky conditions. $Log_{10}\varepsilon$ is found to be linearly correlated with $T_s - T_a$ (and VWS) (p<0.05). The surface sensible heat flux generally increases with increased $T_s - T_a$, thus the increased $T_s - T_a$ intensifies the turbulence in PBL (0<z/z_i<1.0), which is shown in Fig. 6b, e, h. Within the PBL, ε is also positively correlated with $T_s - T_a$ whose slope values are larger than those at 0.2<z/z_i<2.0. As $T_s - T_a$ rises, the larger surface sensible heat flux would lead to enhanced buoyancy process and turbulent motion within the PBL. On the other hand, ε above the PBL is negatively correlated with $T_s - T_a$(Figs. 6c, f, i). This suggests that $T_s - T_a$ dramatically affects the development of turbulence within the PBL, whereas it has little effect on the turbulence above the PBL.

Within the PBL, the magnitude of slope (slope=0.019) under clear-sky conditions is larger than that of under-cloudy conditions (slope = 0.015) as shown in Figs. 6e and 6h. This implies that $T_s - T_a$ is one of the dominant factors affecting the PBL turbulence, particularly under the clear-sky conditions. Given that turbulence in the mixed PBL over the TP is usually driven by convection (Xu et al., 2023), as $T_s - T_a$ decreases when clouds are present, less heat is transferred from the surface to the atmosphere, reducing the buoyancy flux and leading to weaker turbulence in the PBL, especially for the lower PBL (0.2<z/z_i<0.5), as shown in Figures 4b and 4c. Consequently, the clouds tend to suppress the development of PBL (Fig. 5a) and reduce z_i.

https://doi.org/10.5194/egusphere-2024-860
Preprint. Discussion started: 11 April 2024

3.2.2 Vertical wind shear

Besides $T_s - T_a$, VWS is another crucial dynamic parameter that is related to the mechanical turbulence within the PBL. Similar to Fig. 6, Figure 7 presents the relationship between ε and VWS (both normalized by z_i) within and above the PBL under all-, clear- and cloudy-sky conditions, respectively. The near-surface clutter significantly increases the uncertainty of RWP data, which leads to incapability of analyzing the effect of wind shear on ε below 0.5 km AGL in the following sections.

Regardless of within or above the PBL, ε is positively correlated with VWS as shown in Fig. 7a, d, g and Tabel 2, which indicates that larger VWS leads to stronger turbulence. This suggests that the dynamic effect of VWS promotes the development of turbulence. Within the PBL (Figs. 7b, e, h), the slope of ε against VWS are smaller than at 0.2<z/z_i<2.0 with values ranging from 9.5 to 10.3. Above the PBL (Figs. 7c, f, i), the values of the slope are larger with values ranging from 10.7 to 18.1, which demonstrating that the dynamical effects of VWS influence the development of turbulence both within and above the PBL.

Under cloudy-sky conditions (Figs. 7h, i), the effect of VWS on turbulence within the PBL (Slope =10.3) is weaker than above the PBL (Slope=18.1), significantly. Compared to the clear-sky conditions (Figs. 7e, f), the values of the slopes are larger for that of under cloudy-sky conditions (Figs. 7h, i) both within and above the PBL. Remarkably, above the PBL, the effect of clouds on turbulence is more dramatic, as the slope value under cloudy-sky conditions is nearly twice as large as that of under clear-sky conditions. These results indicate the significant mechanical processes driven by VWS is important in the development of turbulence. A larger VWS in the PBL corresponds to stronger turbulence. Besides, above the PBL, the mechanical process of VWS is enhanced under cloudy-sky conditions.

3.2.3. Joint influence of $T_s - T_a$, VWS and atmosphere stability on ε

It was stated that turbulence can be produced by buoyant convective processes (i.e., thermals of warm air rising) and by mechanical processes (i.e., wind shear). From the

https://doi.org/10.5194/egusphere-2024-860
Preprint. Discussion started: 11 April 2024

previous section, it is known that $T_s - T_a$ and VWS both affect the development of PBL turbulence. Figure 8 gives the slope profiles of ε against $T_s - T_a$ and VWS at normalized heights (z/z_i) under all-, clear- and cloudy-sky conditions, respectively.

As inferred from the previous findings, $T_s - T_a$ primarily influences turbulence development within the PBL, irrespective of clear-sky and cloudy-sky conditions (Fig. 6). Figure 8a shows that the slope values within the PBL are predominantly positive, and the slope value decreases rapidly with height, which indicates that the influence of $T_s - T_a$ on PBL turbulence experiences decreasing trend with height. Interestingly, there is a nearly linear of slope value from the lower PBL to a smaller positive value near the top of the PBL. Above the PBL, the slope value becomes negative. This may be due to the linear decrease of heat flux transport and buoyancy term in the convective PBL (Stull, 1988). Therefore, these findings highlight the predominant thermal forcing of $T_s - T_a$ on turbulence development within the lower PBL. In addition, when 0.2<z/z_i<0.5, the slope values are larger for clear-sky conditions than for cloudy-sky conditions, while there is little difference for the clear-sky and cloudy-sky conditions when 0.5<z/z_i. Hence, under clear-sky conditions, the thermodynamic effect of $T_s - T_a$ is more pronounced within the lower PBL.

As shown in Fig. 7, it is evident that VWS influences turbulence development within and above the PBL. Figure 8b shows that when 0.2<z/z_i <2.0, the slope values are consistently positive, indicating that VWS predominantly affects turbulence development within the mid-, upper- PBL and above the PBL. Moreover, when 0.2<z/z_i<1.2, the slope values increase with height. However, when 1.4<z/z_i<2.0, the slope values exhibit a decreasing trend, which suggesting a diminishing influence of VWS. Additionally, within the PBL (0.2<z/z_i<0.7), the slope values under clear-sky conditions are close to those under cloudy-sky conditions, while the slope values under cloudy-sky conditions are even greater when 0.7<z/z_i<2.0. For instance, when z/z_i=1.4, $\mathrm{Slope}_{\mathrm{Clear\text{-}sky}}$=14.6, while $\mathrm{Slope}_{\mathrm{Cloudy\text{-}sky}}$=27.0, indicating that the latter is 1.8 times larger than the former. These results suggest that clouds are primarily responsible for enhancing mechanical processes from VWS on turbulence within the upper PBL and above the PBL.

https://doi.org/10.5194/egusphere-2024-860
Preprint. Discussion started: 11 April 2024

Furthermore, it can be concluded that, $T_s - T_a$ is the thermodynamic factor influencing turbulence development within the lower PBL (0.2<z/z_i<0.5), both $T_s - T_a$ and VWS jointly strengthen turbulence development in the upper PBL (0.6<z/z_i<1.0), and VWS emerges as the predominant factor affecting turbulence development above the PBL (1.0<z/z_i<2.0) (Figs. 8a, b).

The previous sections have revealed that hours of both high $T_s - T_a$ and strong wind shear would strengthen the turbulence within the PBL. Therefore, it's necessary to analyze the combined influence of thermodynamics and dynamics factors on the development of turbulence. Figure 9 presents the joint distribution of ε with $T_s - T_a$ and VWS within and above the PBL under all-, clear- and cloudy-sky conditions. Within the PBL (Figs. 9b, e, h), higher $T_s - T_a$ and VWS correspond to stronger turbulence (Fig. 8). In contrast, the thermodynamic effect of $T_s - T_a$ on turbulence has diminished and is no longer a dominant factor above the PBL, while the dynamical effect of VWS becomes the dominant factor (Figs. 9c, f, i). Compared to clear-sky conditions, both $T_s - T_a$ and VWS decrease under cloudy-sky conditions (Fig. 9h). This means that the weakening of both thermodynamic and dynamic effects leads to a decrease in turbulence, thereby inhibiting the development of turbulence within the PBL. Therefore, under cloudy-sky conditions, although the VWS is reduced, the dynamical effect of VWS on turbulence is strengthened (Figs. 7i and 8b), which in turn strengthens turbulence.

Since buoyant and mechanistic forcing jointly influence the turbulence within the PBL, and VWS only represents the dynamic driving effect, it cannot accurately portray the effect of thermodynamic and dynamic effects on the PBL turbulence. The gradient Richardson number (Ri), on the other hand, is one of the important parameters characterizing atmospheric stability and can compare the buoyant turbulence production term and the shear production term in the form of a dimensionless ratio.

Similar to Fig. 9, the joint distribution of ε with $T_s - T_a$ and Ri within and above the PBL under all-sky, clear-sky and cloudy-sky conditions is given in Fig. 10. Within the PBL (Figs. 10b, e, h), it is evident that the turbulence in the PBL is enhancing for unstable conditions. Furthermore, under clear-sky conditions (Fig. 10e), the maximum number of samples is found when Ri<1.0 and $T_s - T_a$>21.1 in strongly unstable conditions caused

https://doi.org/10.5194/egusphere-2024-860
Preprint. Discussion started: 11 April 2024

by the buoyancy forcing driven by the larger $T_s - T_a$. While the effect of Ri on turbulence is relatively weakened above the PBL (Figs. 10c, f, i).

4 Summary and concluding remarks

This study investigates the characteristics of spatio-temporal distribution of daytime PBL turbulence dissipation rate (ε) based on more than one-year record (September 2022–October 2023) of profiling measurements from a radar wind profilers (RWP) network on the Tibet Plateau (TP). Also analyzed are the evolution of ε in the PBL and the possible influential mechanisms.

First of all, ε is firstly retrieved from the vertical wind measurements from RWP using the spectral width method. Afterwards, the spatial pattern of ε is examined. Results shows that the values of ε at both Minfeng and Jiuquan sites in the northern TP, and at Dingri over the southern TP are about one order of magnitude greater than those at the RWP sites of Lijiang, Ganzi and Hongyuan over the eastern TP. Coincidently, Minfeng and Junquan are dominated by bare or semiarid land, as opposed to the highly vegetation-covered land surface at Lijiang, Ganzi and Hongyuan. This suggests the spatial discrepancy of ε over the TP is highly relevant to the types of underlying land cover.

Although ε exhibits a variety of magnitudes among the six RWPs, the daytime pattern and vertical structure of ε are similar. Turbulence reaches the peak in the early afternoon (1300–1500 LST), coinciding with the highest PBL top. Under cloudy-sky conditions, the daytime mean value of ε is $10^{-4.02}$ m^2 s^{-3}, and the daytime mean value of the PBL height (z_i) can reach up to 1415 m, which is 117 m lower than that of clear-sky conditions, indicating that clouds would suppress the development of the PBL turbulence.

As far as both the thermodynamic and dynamic forcings are concerned, surface-air temperature difference ($T_s - T_a$) and vertical wind shear (VWS) variables are examined by performing correlation analysis with ε. The slope values of ε against $T_s - T_a$ under clear-sky conditions is larger (slope=0.019) than under-cloudy conditions (slope = 0.013) within the PBL, while those values are negative above the PBL. The slope values of ε against VWS is positive regardless of within or above the PBL, where the largest value of 18.1 is

https://doi.org/10.5194/egusphere-2024-860
Preprint. Discussion started: 11 April 2024

observed above the PBL under cloudy-sky conditions, and the smallest value of 9.5 is observed in the PBL within clear-sky conditions.

Both the thermodynamic effect of $T_s - T_a$ and the dynamic effect of VWS enhance the development of turbulence under clear-sky or cloudy-sky conditions in the PBL. In the lower PBL (0.2<z/z_i<0.5), $T_s - T_a$ has a larger positive slope with ε, which suggests that thermal forcing emerges as the dominant factor influencing development of the turbulence and PBL. By comparison, in the upper PBL (0.6<z/z_i<1.0), $T_s - T_a$ and VWS jointly influence the development of turbulence, with larger $T_s - T_a$ leading to unstable atmospheric stability and stronger turbulence. Above the PBL (1.0<z/z_i<2.0), VWS becomes the dominant factor influencing the development of turbulence. Compared to clear-sky conditions, on one hand, clouds would diminish $T_s - T_a$, resulting in decreased heat transfer from the surface to the PBL top, thereby weakening turbulence within the lower PBL (0.2<z/z_i<0.5), inhibiting PBL development, and decreasing z_i. On the other hand, the stronger wind shear process would enhance the turbulence above PBL under the cloudy-sky conditions.

Although the above-mentioned findings of the PBL turbulence over the TP are the first results from profiling network observations to the best of our knowledge, fine-resolution spatial distribution remains unclear, largely due to the sparse distribution of RWP network on the TP. On top of this, the role of roughness length remains known in the variation and evolution of turbulence, especially in the lowest part of PBL, which warrants a field campaign involved in the high-density turbulence observation network along with high-resolution satellite images.

Data Availability

The authors would like to acknowledge the National Meteorological Information Centre (NMIC) of China Meteorological Administration (CMA) (https://data.cma.cn) for providing the high-resolution radar wind profiler and ground-based meteorological data,

which can be only accessed via registration. We are grateful to ECMWF for providing ERA5 hourly data (https://www.ecmwf.int/en/forecasts/datasets/reanalysis-datasets/era5/).

Acknowledgments

This work was jointly supported by the National Natural Science Foundation of China under grants 42325501, U2142209 and 42105090. Last but not least, we appreciated tremendously the constructive comments and suggestions made by the anonymous reviewers that significantly improved the quality of our manuscript.

Author Contributions

The study was completed with close cooperation between all authors. JG conceived of the idea for this work. DM performed the analysis, DM and JG drafted the original manuscript with contributions from XG, NL, YS, ZZ and NT. YW, HL, FZ, BT, HX and TC provided useful suggestions and comments for the study and helped revise the manuscript.

Completing interests

The authors declare that they have no conflict of interest.

References

Adler, B. and Kalthoff, N.: Multi-scale transport processes observed in the boundary layer over a mountainous island, Bound.-Layer Meteor., 153, 515-537, https://doi.org/10.1007/s10546-014-9957-8, 2014.

Banerjee, T., Brugger, P., De Roo, F., Kröniger, K., Yakir, D., Rotenberg, E., and Mauder, M.: Turbulent transport of energy across a forest and a semiarid shrubland, Atmos. Chem. Phys., 18, 10025–10038, https://doi.org/10.5194/acp-18-10025-2018, 2018.

Bianco, L., Wilczak, J. M., and White, A. B.: Convective boundary layer depth estimation from wind profilers: Statistical comparison between an automated algorithm and expert estimations, J. Atmos. Ocean. Technol., 25, 1397-1413, https://doi.org/10.1175/2008jtecha981.1, 2008.

https://doi.org/10.5194/egusphere-2024-860
Preprint. Discussion started: 11 April 2024

Bodenschatz, E., Malinowski, S. P., Shaw, R. A., and Stratmann, F.: Can we understand clouds without turbulence? Science, 327, 970-971, https://doi.org/10.1126/science.1185138, 2010.

Che, J. H. and Zhao, P.: Characteristics of the summer atmospheric boundary layer height over the Tibetan Plateau and influential factors, Atmos. Chem. Phys., 21, 5253-5268, https://doi.org/10.5194/acp-21-5253-2021, 2021.

Chechin, D. G., Lüpkes, C., Hartmann, J., Ehrlich, A., and Wendisch, M.: Turbulent structure of the Arctic boundary layer in early summer driven by stability, wind shear and cloud-top radiative cooling: ACLOUD airborne observations, Atmos. Chem. Phys., 23, 4685-4707, https://doi.org/10.5194/acp-23-4685-2023, 2023.

Chen, X. L., Añel, J. A., Su, Z. B., de la Torre, L., Kelder, H., van Peet, J., and Ma, Y. M.: The deep atmospheric boundary layer and its significance to the stratosphere and troposphere exchange over the Tibetan Plateau, PLoS One, 8, 9, https://doi.org/10.1371/journal.pone.0056909, 2013.

Chen, X. L., Skerlak, B., Rotach, M. W., Añel, J. A., Su, Z., Ma, Y. M., and Li, M. S.: Reasons for the extremely high-ranging planetary boundary layer over the western Tibetan Plateau in winter, J. Atmos. Sci., 73, 2021-2038, https://doi.org/10.1175/jas-d-15-0148.1, 2016.

Dai, C., Wang, Q., Kalogiros, J. A., Lenschow, D. H., Gao, Z., and Zhou, M.: Determining boundary-layer height from aircraft measurements, Bound.-Layer Meteor., 152, 277-302, https://doi.org/10.1007/s10546-014-9929-z, 2014.

Dodson, D. S. and Griswold, J. D. S.: Turbulent and boundary layer characteristics during VOCALS-REx, Atmos. Chem. Phys., 21, 1937-1961, https://doi.org/10.5194/acp-21-1937-2021, 2021.

Guo, J. P., Li, Y., Cohen, J. B., Li, J., Chen, D. D., Xu, H., Liu, L., Yin, J. F., Hu, K. X., and Zhai, P. M.: Shift in the temporal trend of boundary layer height in China using long-term (1979-2016) radiosonde data, Geophys. Res. Lett., 46, 6080-6089, https://doi.org/10.1029/2019gl082666, 2019.

Guo, J. P., Miao, Y. C., Zhang, Y., Liu, H., Li, Z. Q., Zhang, W. C., He, J., Lou, M. Y., Yan, Y., Bian, L. G., and Zhai, P.: The climatology of planetary boundary layer height

https://doi.org/10.5194/egusphere-2024-860
Preprint. Discussion started: 11 April 2024

in China derived from radiosonde and reanalysis data, Atmos. Chem. Phys., 16, 13309-13319, https://doi.org/10.5194/acp-16-13309-2016, 2016.

Guo, J. P., Liu, B. M., Gong, W., Shi, L. J., Zhang, Y., Ma, Y. Y., Zhang, J., Chen, T. M., Bai, K. X., Stoffelen, A., de Leeuw, G., and Xu, X. F.: First comparison of wind observations from ESA's satellite mission Aeolus and ground-based radar wind profiler network of China, Atmos. Chem. Phys., 21, 2945-2958, https://doi.org/10.5194/acp-21-2945-2021, 2021a.

Guo, J. P., Zhang, J., Yang, K., Liao, H., Zhang, S. D., Huang, K. M., Lv, Y. M., Shao, J., Yu, T., Tong, B., Li, J., Su, T. N., Yim, S. H. L., Stoffelen, A., Zhai, P. M., and Xu, X. F.: Investigation of near-global daytime boundary layer height using high-resolution radiosondes: first results and comparison with ERA5, MERRA-2, JRA-55, and NCEP-2 reanalyses, Atmos. Chem. Phys., 21, 17079-17097, https://doi.org/10.5194/acp-21-17079-2021, 2021b.

Guo, X. R., Guo, J. P., Zhang, D. L., and Yun, Y. X.: Vertical divergence profiles as detected by two wind-profiler mesonets over East China: Implications for nowcasting convective storms, Q. J. R. Meteorol. Soc., 149, 1629-1649, https://doi.org/10.1002/qj.4474, 2023.

Hersbach, H., Bell, B., Berrisford, P., Hirahara, S., Horányi, A., Muñoz-Sabater, J., Nicolas, J., Peubey, C., Radu, R., Schepers, D., Simmons, A., Soci, C., Abdalla, S., Abellan, X., Balsamo, G., Bechtold, P., Biavati, G., Bidlot, J., Bonavita, M., De Chiara, G., Dahlgren, P., Dee, D., Diamantakis, M., Dragani, R., Flemming, J., Forbes, R., Fuentes, M., Geer, A., Haimberger, L., Healy, S., Hogan, R. J., Hólm, E., Janisková, M., Keeley, S., Laloyaux, P., Lopez, P., Lupu, C., Radnoti, G., de Rosnay, P., Rozum, I., Vamborg, F., Villaume, S., and Thépaut, J. N.: The ERA5 global reanalysis, Q. J. R. Meteorol. Soc., 146, 1999-2049, https://doi.org/10.1002/qj.3803, 2020.

Huang, J. P., Zhou, X. J., Wu, G. X., Xu, X. D., Zhao, Q. Y., Liu, Y. M., Duan, A. M., Xie, Y. K., Ma, Y. M., Zhao, P., Yang, S., Yang, K., Yang, H. J., Bian, J. C., Fu, Y. F., Ge, J. M., Liu, Y. Z., Wu, Q. G., Yu, H. P., Wang, B. B., Bao, Q., and Qie, K.: Global climate impacts of land-surface and atmospheric processes over the Tibetan Plateau, Rev. Geophys., 61, 39, https://doi.org/10.1029/2022rg000771, 2023.

https://doi.org/10.5194/egusphere-2024-860
Preprint. Discussion started: 11 April 2024

Jacoby-Koaly, S., Campistron, B., Bernard, S., Bénech, B., Girard-Ardhuin, F., Dessens, J., Dupont, E., and Carissimo, B.: Turbulent dissipation rate in the boundary layer via UHF wind profiler Doppler spectral width measurements, Bound.-Layer Meteor., 103, 361-389, https://doi.org/10.1023/a:1014985111855, 2002.

Kotthaus, S., Bravo-Aranda, J. A., Coen, M. C., Guerrero-Rascado, J. L., Costa, M. J., Cimini, D., O'Connor, E. J., Hervo, M., Alados-Arboledas, L., Jiménez-Portaz, M., Mona, L., Ruffieux, D., Illingworth, A., and Haeffelin, M.: Atmospheric boundary layer height from ground-based remote sensing: a review of capabilities and limitations, Atmos. Meas. Tech., 16, 433-479, https://doi.org/10.5194/amt-16-433-2023, 2023.

Lai, Y., Chen, X. L., Ma, Y. M., Chen, D. L., and Zhaxi, S. L.: Impacts of the westerlies on planetary boundary layer growth over a valley on the north side of the Central Himalayas, J. Geophys. Res.-Atmos., 126, 20, https://doi.org/10.1029/2020jd033928, 2021.

Li, Y., Y. Wu, J. Tang, P. Zhu, Z. Gao, and Y. Yang. Quantitative evaluation of wavelet analysis method for turbulent flux calculation of non-stationary series, Geophys. Res. Lett., 50(5), e2022GL101591, http://dx.doi.org/10.1029/2022GL101591, 2023.

Li, Z. G., Lyu, S. H., Wen, L. J., Zhao, L., Ao, Y. H., and Wang, S. Y.: Effect of a cold, dry air incursion on atmospheric boundary layer processes over a high-altitude lake in the Tibetan Plateau, Atmos. Res., 185, 32-43, https://doi.org/10.1016/j.atmosres.2016.10.024, 2017a.

Li, Z. Q., Guo, J. P., Ding, A. J., Liao, H., Liu, J. J., Sun, Y. L., Wang, T. J., Xue, H. W., Zhang, H. S., and Zhu, B.: Aerosol and boundary-layer interactions and impact on air quality, Natl. Sci. Rev., 4, 810-833, https://doi.org/10.1016/10.1093/nsr/nwx117, 2017b.

Liu, B. M., Guo, J. P., Gong, W., Shi, L. J., Zhang, Y., and Ma, Y. Y.: Characteristics and performance of wind profiles as observed by the radar wind profiler network of China, Atmos. Meas. Tech., 13, 4589-4600, https://doi.org/10.5194/amt-13-4589-2020, 2020.

Liu, B. M., Ma, Y. Y., Guo, J. P., Gong, W., Zhang, Y., Mao, F. Y., Li, J., Guo, X. R., and Shi, Y. F.: Boundary layer heights as derived from ground-based radar wind profiler

https://doi.org/10.5194/egusphere-2024-860
Preprint. Discussion started: 11 April 2024

in Beijing, IEEE Trans. Geosci. Remote Sensing, 57, 8095-8104, https://doi.org/10.1109/tgrs.2019.2918301, 2019.

Lv, Y. M., Guo, J. P., Li, J., Cao, L. J., Chen, T. M., Wang, D., Chen, D. D., Han, Y., Guo, X. R., Xu, H., Liu, L., Solanki, R., and Huang, G.: Spatiotemporal characteristics of atmospheric turbulence over China estimated using operational high-resolution soundings, Environ. Res. Lett., 16, 13, https://doi.org/10.1088/1748-9326/abf461, 2021.

Ma, Y. M., Yao, T. D., Zhong, L., Wang, B. B., Xu, X. D., Hu, Z. Y., Ma, W. Q., Sun, F. L., Han, C. B., Li, M. S., Chen, X. L., Wang, J. M., Li, Y. Q., Gu, L. L., Xie, Z. P., Liu, L., Sun, G. H., Wang, S. J., Zhou, D. G., Zuo, H. C., Xu, C., Liu, X., Wang, Y. J., and Wang, Z. Y.: Comprehensive study of energy and water exchange over the Tibetan Plateau: A review and perspective: From GAME/Tibet and CAMP/Tibet to TORP, TPEORP, and TPEITORP, Earth-Sci. Rev., 104312, 2023.

McCaffrey, K., Bianco, L., and Wilczak, J. M.: Improved observations of turbulence dissipation rates from wind profiling radars, Atmos. Meas. Tech., 10, 2595-2611, https://doi.org/10.5194/amt-10-2595-2017, 2017.

Muhsin, M., Sunilkumar, S. V., Ratnam, M. V., Parameswaran, K., Murthy, B. V. K., Ramkumar, G., and Rajeev, K.: Diurnal variation of atmospheric stability and turbulence during different seasons in the troposphere and lower stratosphere derived from simultaneous radiosonde observations at two tropical stations, in the Indian Peninsula, Atmos. Res., 180, 12-23, https://doi.org/10.1016/j.atmosres.2016.04.021, 2016.

Muñoz-Esparza, D., Sharman, R. D., and Lundquist, J. K.: Turbulence Dissipation Rate in the Atmospheric Boundary Layer: Observations and WRF Mesoscale Modeling during the XPIA Field Campaign, Mon. Weather Rev., 146, 351-371, https://doi.org/10.1175/mwr-d-17-0186.1, 2018.

Nastrom, G. D.: Doppler radar spectral width broadening due to beamwidth and wind shear, Ann. Geophys.-Atmos. Hydrospheres Space Sci., 15, 786-796, https://doi.org/10.1007/s00585-997-0786-7, 1997.

https://doi.org/10.5194/egusphere-2024-860
Preprint. Discussion started: 11 April 2024

Ruan, Z., Mu, R. Q., Wei, M., and Ge, R. S.: Spectrum analysis of wind profiling radar measurements, J. Meteorol. Res., 28, 656-667, https://doi.org/10.1007/s13351-014-3171-y, 2014.

Schumann, U. and Moeng, C. H.: Plume budgets in clear and cloudy convective boundary layers, J. Atmos. Sci., 48, 1758-1770, https://doi.org/10.1175/1520-0469(1991)048<1758:Pbicac>2.0.Co;2, 1991.

Slättberg, N., Lai, H. W., Chen, X. L., Ma, Y. M., and Chen, D. L.: Spatial and temporal patterns of planetary boundary layer height during 1979-2018 over the Tibetan Plateau using ERA5, Int. J. Climatol., 42, 3360-3377, https://doi.org/10.1002/joc.7420, 2022.

Solanki, R., Guo, J. P., Lv, Y. M., Zhang, J., Wu, J. Y., Tong, B., and Li, J.: Elucidating the atmospheric boundary layer turbulence by combining UHF radar wind profiler and radiosonde measurements over urban area of Beijing, Urban CLim., 43, 13, https://doi.org/10.1016/j.uclim.2022.101151, 2022.

Solanki, R., Guo, J. P., Li, J., Singh, N., Guo, X. R., Han, Y., Lv, Y. M., Zhang, J., and Liu, B. M.: Atmospheric-boundary-layer-height variation over mountainous and urban sites in Beijing as derived from radar wind-profiler measurements, Bound.-Layer Meteor., 181, 125-144, https://doi.org/10.1007/s10546-021-00639-9, 2021.

Stull, R. B.: Mean Boundary Layer Characteristics, in: An Introduction to boundary layer meteorology, edited by: Stull, R. B., Springer Netherlands, Dordrecht, 1–27, https://doi.org/10.1007/978-94-009-3027-8_1, 1988.

Teixeira, J., Piepmeier, J. R., Nehrir, A. R., Ao, C. O., Chen, S. S., Clayson, C. A., Fridlind, A. M., Lebsock, M., McCarty, W., Salmun, H., Santanello, J. A., Turner, D. D., Wang, Z., and Zeng, X.: Toward a global planetary boundary layer observing system: the NASA PBL incubation study team report, NASA PBL Incubation Study Team, 134 pp., available at: https://science.nasa.gov/science-red/s3fs-public/atoms/files/NASAPBLIncubationFinalReport.pdf, last access: 15 November 2021.

Wan, X., Zheng, J. F., Wan, R., Xu, G. R., Qin, J. F., and Yi, L.: Intercomparison of cloud vertical structures over four different sites of the eastern slope of the Tibetan Plateau in summer using Ka-band millimeter-wave radar measurements, Remote Sens., 14, 19, https://doi.org/10.3390/rs14153702, 2022.

https://doi.org/10.5194/egusphere-2024-860
Preprint. Discussion started: 11 April 2024

Wang, C. X., Ma, Y. M., and Han, C. B.: Research on the atmospheric boundary layer structure and its development mechanism in the Tibetan Plateau, Adv. Atmos. Sci., 38, 414-428, 2023a.

Wang, M. Z. and Zhang, J. T.: The relationship among summer atmospheric boundary layer height over the Taklimakan Desert, its land surface parameters and Eurasian circulation, Atmos. Sci. Lett., 23, 13, https://doi.org/10.1002/asl.1122, 2022.

Wang, M. Z., Lu, H., Ming, H., and Zhang, J. T.: Vertical structure of summer clear-sky atmospheric boundary layer over the hinterland and southern margin of Taklamakan Desert, Meteorol. Appl., 23, 438-447, https://doi.org/10.1002/met.1568, 2016.

Wang, S. Q., Guo, J. P., Xian, T., Li, N., Meng, D. L., Li, H. J., and Cheng, W.: Investigation of low-level supergeostrophic wind and Ekman spiral as observed by a radar wind profiler in Beijing, Front. Environ. Sci., 11, 9, https://doi.org/10.3389/fenvs.2023.1195750, 2023b.

Wang, Y. J., Zeng, X. B., Xu, X. D., Xie, F. Q., and Zhao, Y.: Improving the estimate of summer daytime planetary boundary layer height over land from GPS radio occultation data, Geophys. Res. Lett., 49, 9, https://doi.org/10.1029/2021gl096304, 2022.

Wang, Y. J., Xu, X. D., Zhao, T. L., Sun, J. H., Yao, W. Q., and Zhou, M. Y.: Structures of convection and turbulent kinetic energy in boundary layer over the southeastern edge of the Tibetan Plateau, Sci. China-Earth Sci., 58, 1198-1209, https://doi.org/10.1007/s11430-015-5054-1, 2015.

Wang, Y. J., Zeng, X. B., Xu, X. D., Welty, J., Lenschow, D. H., Zhou, M. Y., and Zhao, Y.: Why are there more summer afternoon low clouds over the Tibetan Plateau compared to eastern China? Geophys. Res. Lett., 47, 10, https://doi.org/10.1029/2020gl089665, 2020.

White, A. B., Lataitis, R. J., and Lawrence, R. S.: Space and time filtering of remotely sensed velocity turbulence, J. Atmos. Ocean. Technol., 16, 1967-1972, https://doi.org/10.1175/1520-0426(1999)016<1967:Satfor>2.0.Co;2, 1999.

Wu, J. Y., Guo, J. P., Yun, Y. X., Yang, R. F., Guo, X. R., Meng, D. L., Sun, Y. P., Zhang, Z., Xu, H., and Chen, T. M.: Can ERA5 reanalysis data characterize the pre-storm

https://doi.org/10.5194/egusphere-2024-860
Preprint. Discussion started: 11 April 2024

environment? Atmos. Res., 297, 18, https://doi.org/10.1016/j.atmosres.2023.107108, 2024.

Xu, L. J., Liu, H. Z., Du, Q., and Xu, X. D.: The assessment of the planetary boundary layer schemes in WRF over the central Tibetan Plateau, Atmos. Res., 230, 12, https://doi.org/10.1016/j.atmosres.2019.104644, 2019.

Xu, X. D., Tang, Y., Wang, Y. J., Zhang, H. S., Liu, R. X., and Zhou, M. Y.: Triggering effects of large topography and boundary layer turbulence on convection over the Tibetan Plateau, Atmos. Chem. Phys., 23, 3299-3309, https://doi.org/10.5194/acp-23-3299-2023, 2023.

Xu, X. D., Zhou, M. Y., Chen, J. Y., Bian, L. G., Zhang, G. Z., Liu, H. Z., Li, S. M., Zhang, H. S., Zhao, Y. J., Suolong, D.J., and Wang, J. Z.: A comprehensive physical pattern of land-air dynamic and thermal structure on the Qinghai-Xizang Plateau, Sci. China Ser. D-Earth Sci., 45, 577-594, https://doi.org/10.1360/02yd9060, 2002.

Yang, B., Qian, Y., Berg, L. K., Ma, P. L., Wharton, S., Bulaevskaya, V., Yan, H. P., Hou, Z. S., and Shaw, W. J.: Sensitivity of Turbine-Height Wind Speeds to Parameters in Planetary Boundary-Layer and Surface-Layer Schemes in the Weather Research and Forecasting Model, Bound.-Layer Meteor., 162, 117-142, https://doi.org/10.1007/s10546-016-0185-2, 2017.

Yang, R. F., Guo, J. P., Deng, W. L., Li, N., Fan, J. H., Meng, D. L., Liu, Z., Sun, Y. P., Zhang, G. L., and Liu, L. H.: Investigation of turbulent dissipation rate profiles from two radar wind profilers at plateau and plain stations in the north China plain, Remote Sens., 15, 14, https://doi.org/10.3390/rs15164103, 2023.

Zhang, L., Zhang, H. S., Li, Q. H., Wei, W., Cai, X. H., Song, Y., Mamtimin, A., Wang, M. Z., Yang, F., Wang, Y., and Zhou, C. L.: Turbulent mechanisms for the deep convective boundary layer in the Taklimakan desert, Geophys. Res. Lett., 49, 9, https://doi.org/10.1029/2022gl099447, 2022.

Zhang, Y., Guo, J. P., Yang, Y. J., Wang, Y., and Yim, S. H. L.: Vertica wind shear modulates particulate matter pollutions: a perspective from radar wind profiler observations in Beijing, China, Remote Sens., 12, 17, https://doi.org/10.3390/rs12030546, 2020.

Zhao, P., Li, Y. Q., Guo, X. L., Xu, X. D., Liu, Y. M., Tang, S. H., Xiao, W. M., Shi, C. X., Ma, Y. M., Yu, X., Liu, H. Z., Jia, L., Chen, Y., Liu, Y. J., Li, J., Luo, D. B., Cao, Y. C., Zheng, X. D., Chen, J. M., Xiao, A., Yuan, F., Chen, D. H., Pang, Y., Hu, Z. Q., Zhang, S. J., Dong, L. X., Hu, J. Y., Han, S., and Zhou, X. J.: The Tibetan Plateau surface-atmosphere coupling system and its weather and climate effects: the third Tibetan Plateau atmospheric science experiment, J. Meteorol. Res., 33, 375-399, https://doi.org/10.1007/s13351-019-8602-3, 2019.

https://doi.org/10.5194/egusphere-2024-860
Preprint. Discussion started: 11 April 2024

Table list

Table 1. Summary of the geographical conditions and land surface of the six radar wind profiler (RWP) sites over the Tibet Plateau (TP).

RWP site	Latitude (°E)	Longitude (°N)	Elevation (m)	Land cover types
Minfeng	82.69	37.07	1408.9	Bare land
Jiuquan	98.49	39.77	1477.2	Bare land
Dingri	87.07	28.39	4326.0	Grassland
Ganzi	100.00	31.62	3353.0	Bare land, grassland
Hongyuan	102.55	32.79	3465.0	Bare land, grassland
Lijiang	100.22	26.85	2382.4	Bare land, grass land

https://doi.org/10.5194/egusphere-2024-860
Preprint. Discussion started: 11 April 2024

Table 2. Summary of the correlation of $\mathrm{Log}_{10}\varepsilon$ at different altitude ranges under all-, clear- and cloudy-sky conditions with $\mathrm{T_s}-\mathrm{T_a}$ and vertical wind shear (VWS) for all six RWP sites. The superscript * for R indicates that the regression slope is statistically significant at $p < 0.01$.

Conditions	$Log_{10}\varepsilon$ VS $T_s - T_a$	$Log_{10}\varepsilon$ VS VWS
all-sky, 0.2<z/z_i<2.0	y=0.010x–4.05, R= 0.21*	y=13.6x–4.19, R=0.29*
all-sky, 0.2<z/z_i<1.0	y=0.018x–3.70, R=0.29*	y=13.2x–3.77, R=0.20*
all-sky, 1.0<z/z_i<2.0	y=-0.005x–4.20, R=-0.09*	y=17.6x–4.57, R=0.36*
clear-sky, 0.2<z/z_i<2.0	y=0.010x–4.03, R=0.23*	y=10.7x–4.13, R=0.26*
clear -sky, 0.2<z/z_i<1.0	y=0.018x–3.67, R=0.30*	y=11.1x–3.70, R=0.17*
clear -sky, 1.0<z/z_i<2.0	y=-0.006x–4.16, R=-0.12*	y=13.8x–4.52, R=0.34*
cloudy-sky, 0.2<z/z_i<2.0	y=0.009x–4.06, R=0.17*	y=18.5x–4.29, R=0.33*
cloudy-sky, 0.2<z/z_i<1.0	y=0.018x–3.72, R=0.26*	y=15.5x–3.84, R=0.23*
cloudy-sky, 1.0<z/z_i<2.0	y=-0.004x–4.23, R=-0.08*	y=26.2x–4.67, R=0.42*

https://doi.org/10.5194/egusphere-2024-860
Preprint. Discussion started: 11 April 2024

Figures

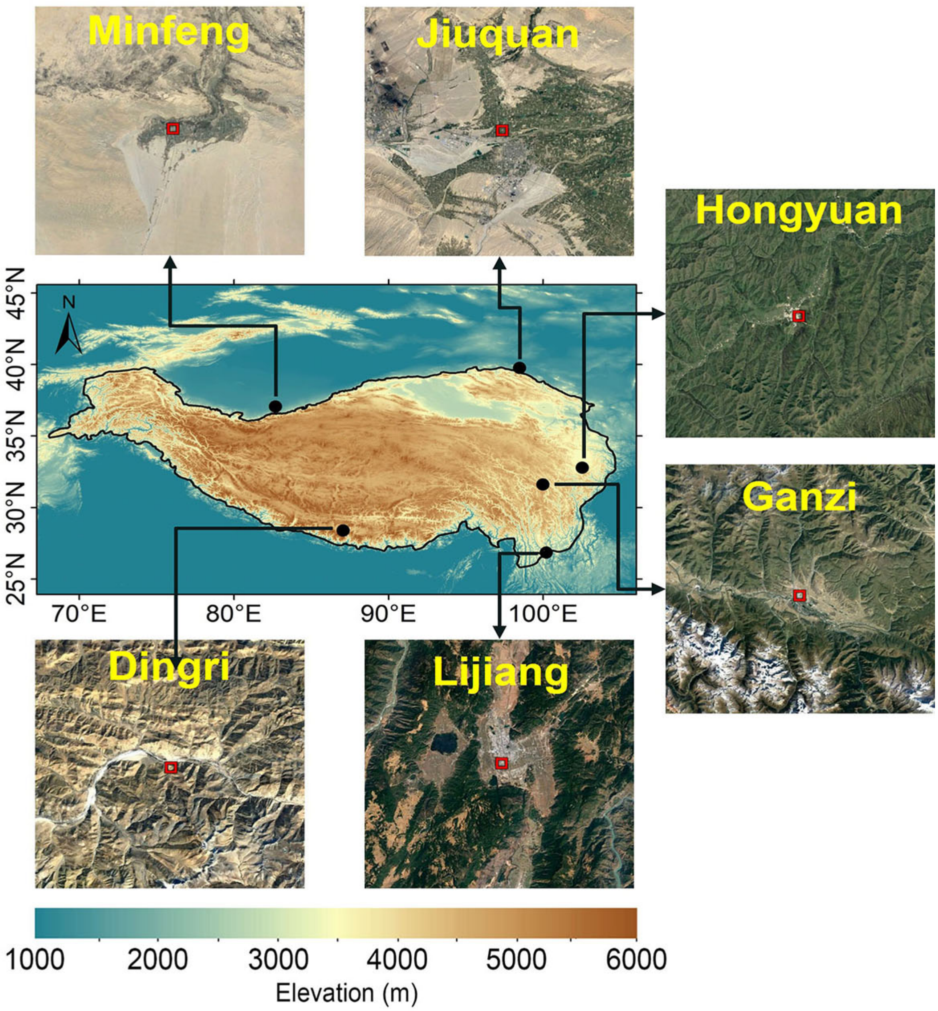

Figure 1. Spatial distribution of radar wind profiler (RWP) network comprised of six sites (in black solid circles) on the Tibetan Plateau (TP). The inset map surrounding the main frame denotes the RGB satellite image from © Google Earth that is centered at each RWP site.

https://doi.org/10.5194/egusphere-2024-860
Preprint. Discussion started: 11 April 2024

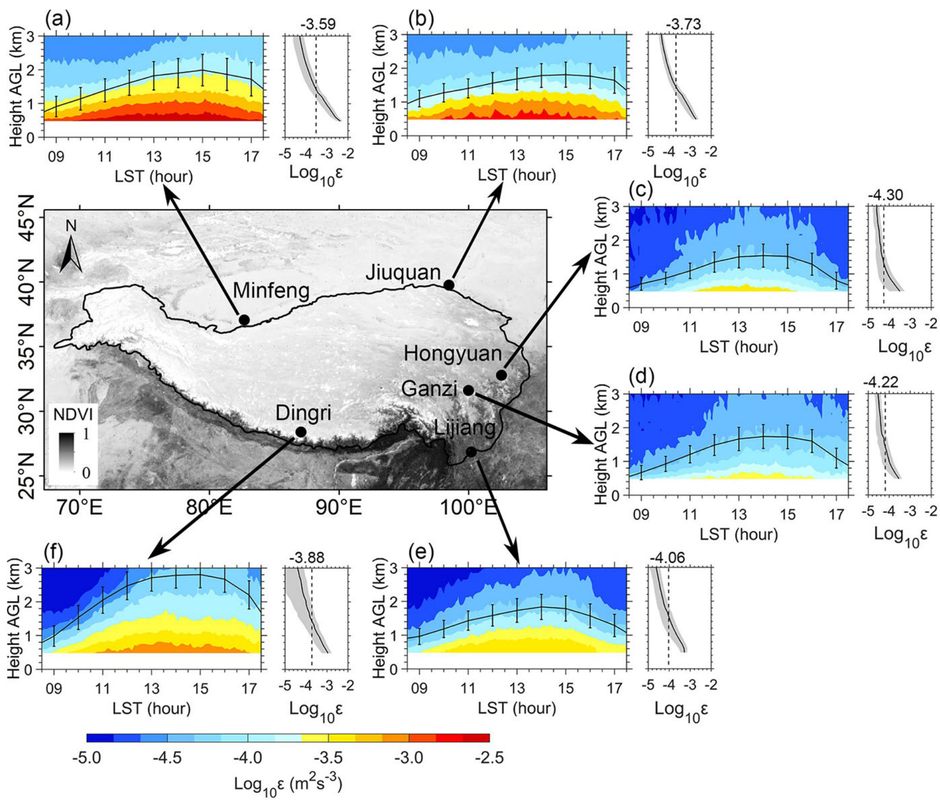

Figure 2. Spatial distribution of the diurnal evolution of the vertical profile of logarithmic turbulence dissipation rate ($Log_{10}\varepsilon$ in color shading, unit: m^2 s^{-3}) at 120 m vertical resolution and 6 min intervals, and hourly mean planetary boundary layer height (z_i, black line, unit: km) during daytime under all-sky conditions from 0900 to 1700 LST for the period September 2022 to October 2023 as retrieved from the profiling measurements at six RWP sites over the TP. The vertical bars indicate the 0.5 standard deviations for z_i. Also shown on the right-hand side panel are temporally averaged vertical profile of ε (black line) and its corresponding one standard deviation (gray shading).

https://doi.org/10.5194/egusphere-2024-860
Preprint. Discussion started: 11 April 2024

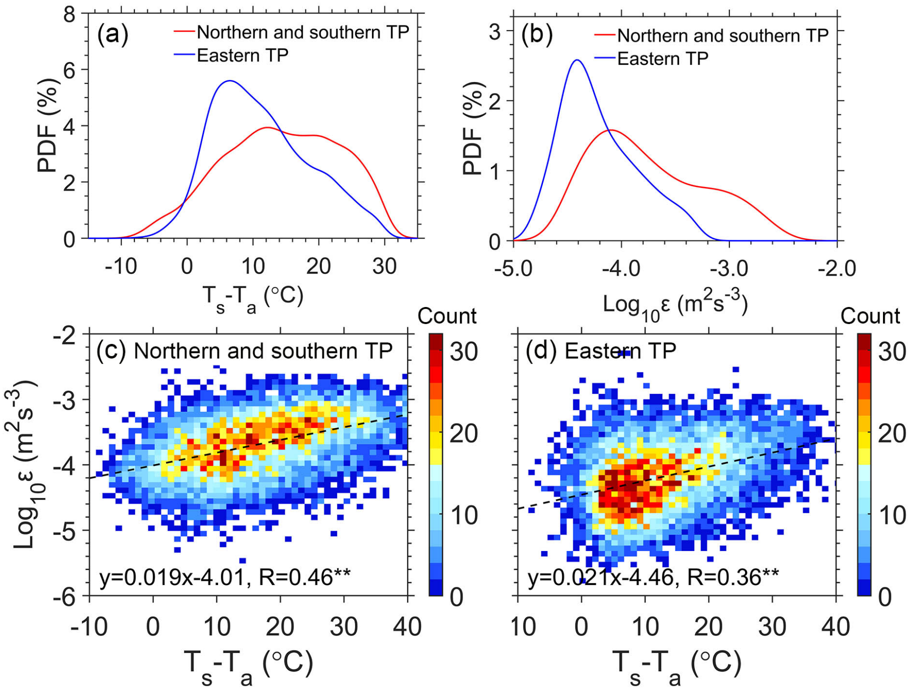

Figure 3. (a) PDF of surface-air temperature difference ($T_s - T_a$) for the northern and southern TP (red line) and eastern TP (blue line), (b) same as (a), but for PDF of Log_{10}ε estimated from the measurements of radar wind profilers (RWPs) at the height below 0.5 km and above 5 km, (c) scatter plots of Log_{10}ε as a function of $T_s - T_a$ in the northern and southern TP, (d) same as (c), but for the eastern TP during daytime under all-sky conditions from 0900 to 1700 local standard time (LST) for the period September 2022 to October 2023. The superscript ** for R indicates that the regression slope is statistically significant at $p < 0.01$ level.

https://doi.org/10.5194/egusphere-2024-860
Preprint. Discussion started: 11 April 2024

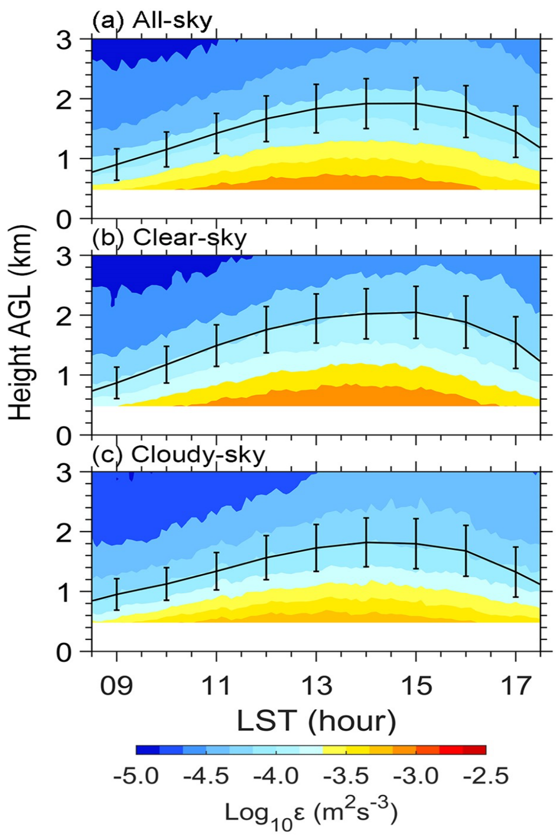

Figure 4. Diurnal evolution of the vertical profile of $Log_{10}\varepsilon$ (color shading, unit: m^2 s^{-3}) and z_i (solid line, unit: km) averaged over the six RWP sites over the TP during daytime from 0900 to 1700 LST for the period September 2022 to October 2023 for (a) all-sky conditions, (b) clear-sky conditions and (c) cloudy-sky conditions. The vertical bars indicate the 0.5 standard deviations.

https://doi.org/10.5194/egusphere-2024-860
Preprint. Discussion started: 11 April 2024

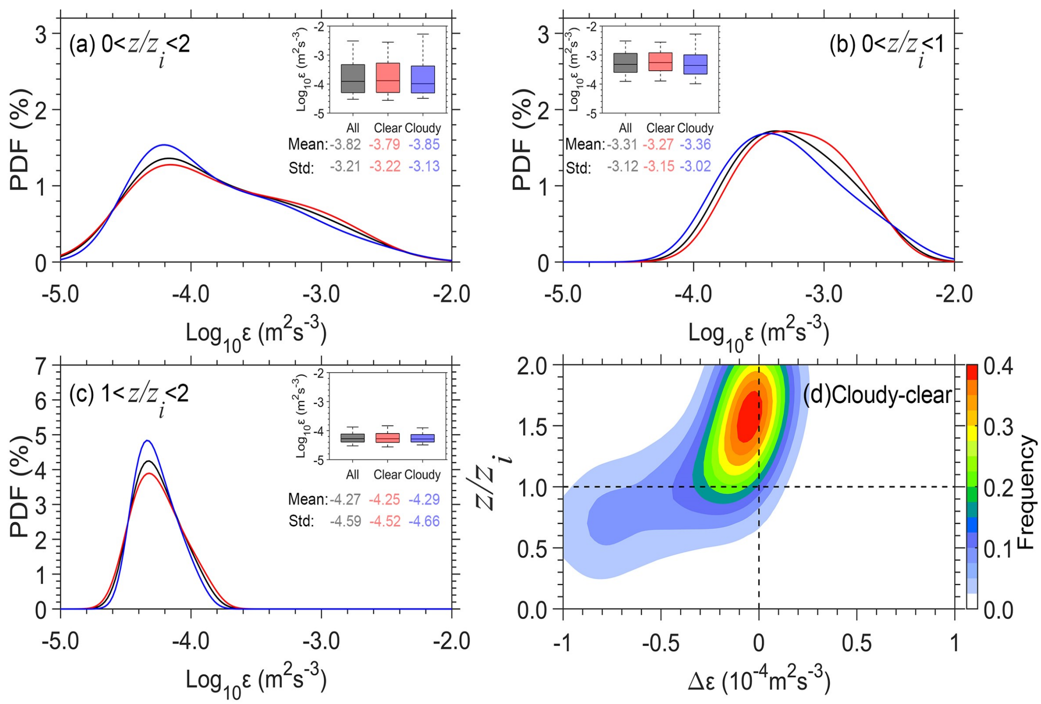

Figure 5. PDF of daytime $Log_{10}\varepsilon$ (a) in the whole lower troposphere (0.2<z/z_i<2.0), (b) in the PBL (0.2<z/z_i<1.0) and (c) above the PBL (1.0<z/z_i<2.0) over the TP under all-sky (black), clear-sky (red) and cloudy-sky (blue) conditions, respectively. (d) Normalized contoured frequency by altitude diagram (NCFAD) for the difference of ε between cloudy-sky and clear-sky conditions (Δε) over the TP. Note that z_i denotes the depth of the PBL, the height (z) and turbulence dissipation rate (ε) is normalized by z_i in order to give a nondimensional vertical coordinate in the form of z/z_i.

https://doi.org/10.5194/egusphere-2024-860
Preprint. Discussion started: 11 April 2024

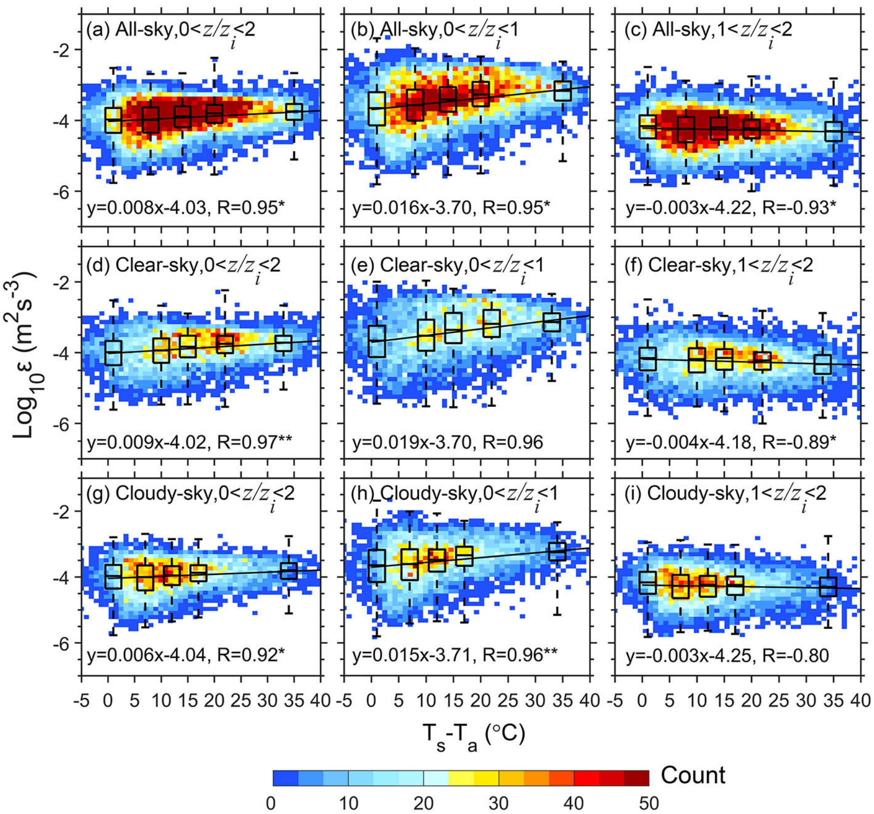

Figure 6. Scatter plots (blue dots) of $Log_{10}\varepsilon$ estimated from the measurements of RWPs in the whole lower troposphere (0.2<z/z_i<2.0, a, d, g), in the PBL (0.2<z/z_i<1.0, b, e, h) and above the PBL (1.0<z/z_i<2.0, c, f, i) over the TP as a function of $T_s - T_a$ under all-sky (a-c), clear-sky (d-f) and cloudy-sky conditions (g-i), respectively. Also overlaid are their corresponding box and whisker plots and regression linear equations and correlation coefficients in each panel, where all $T_s - T_a$ samples are divided into five bins, each of which has the same sample size. Note that the median is shown as a line whereas the outer boundaries of the boxes represent 25 and 75 quartiles and the dashed lines present interquartile range (IQR). The superscripts * and ** for R indicate that the regression slopes are statistically significant at $p < 0.05$ and $p < 0.01$ levels, respectively.

https://doi.org/10.5194/egusphere-2024-860
Preprint. Discussion started: 11 April 2024

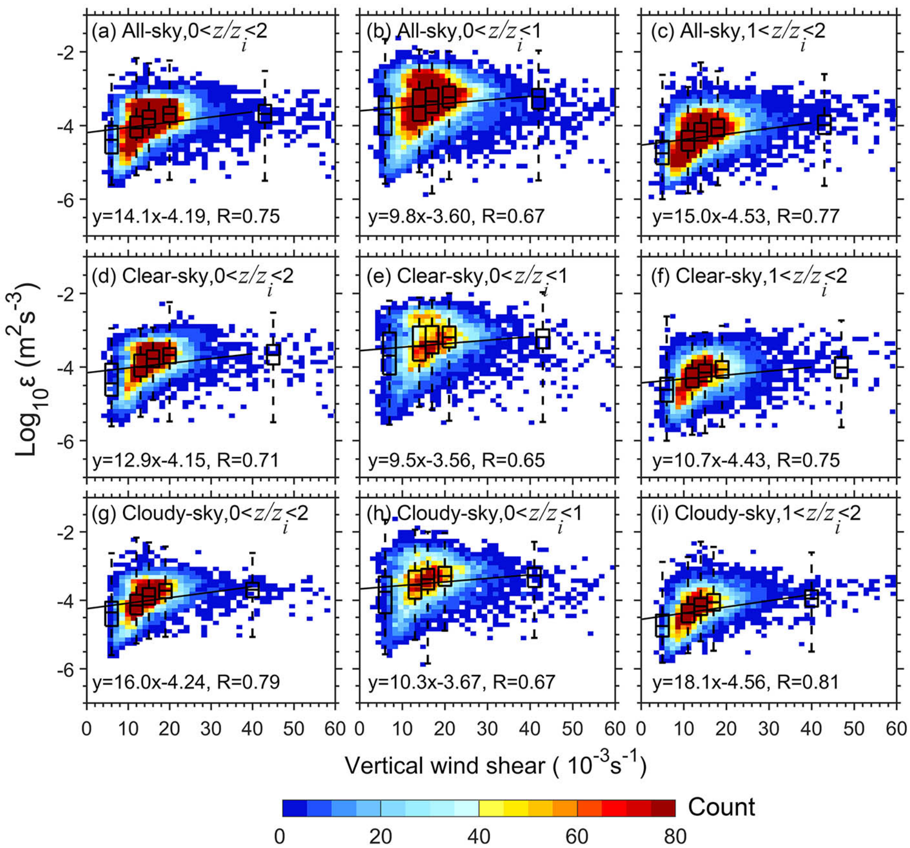

824
825 **Figure 7.** Same as Figure 5, but for $Log_{10}\varepsilon$ as a function of vertical wind shear (VWS).
826

https://doi.org/10.5194/egusphere-2024-860
Preprint. Discussion started: 11 April 2024

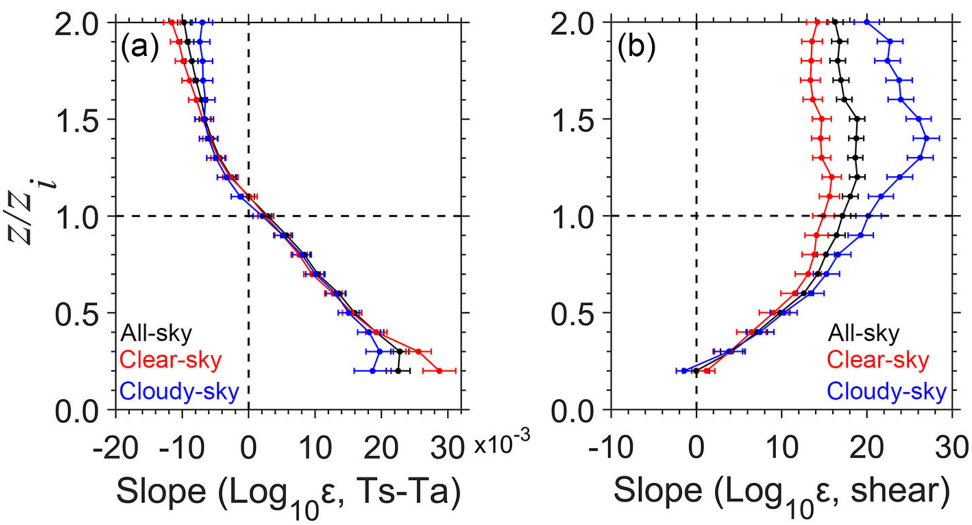

Figure 8. The vertical profiles of least squares regression slope between $Log_{10}\varepsilon$ and $T_s - T_a$ (a) and vertical wind shear (b) over the TP under all-sky (black), clear-sky (red) and cloudy-sky (blue) conditions, respectively.

https://doi.org/10.5194/egusphere-2024-860
Preprint. Discussion started: 11 April 2024

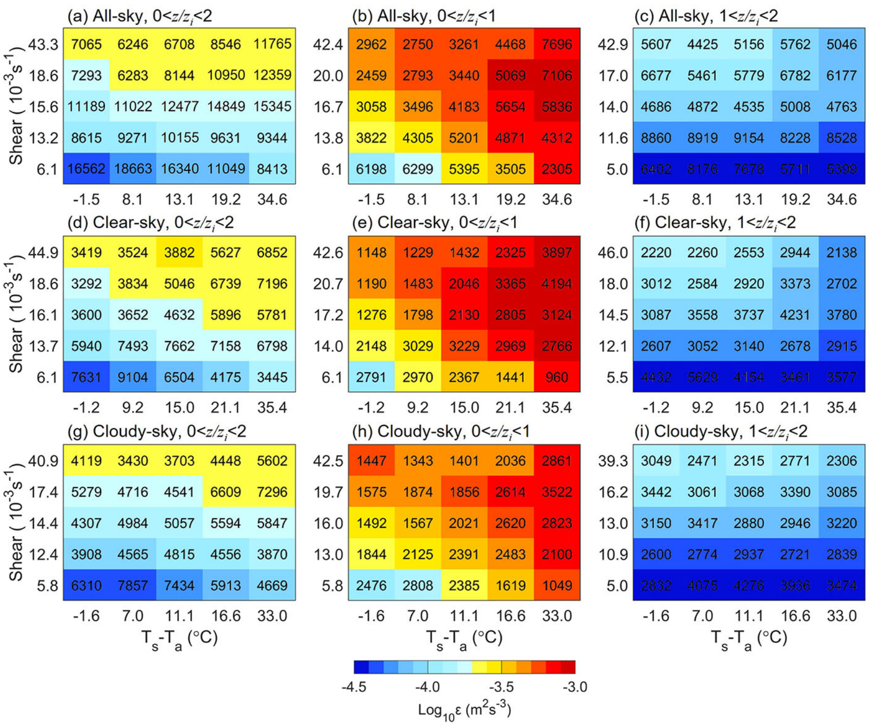

Figure 9. Joint dependence of $Log_{10}\varepsilon$ (color shading) on the vertical wind shear and $T_s - T_a$ within and above the PBL (a, d, g), in the PBL (b, e, h) and above the PBL (c, f, i) over the TP under all-sky (a-c), clear-sky (d-f) and cloudy-sky (g-i) conditions, respectively. The number given in each panel is the total number of samples used.

https://doi.org/10.5194/egusphere-2024-860
Preprint. Discussion started: 11 April 2024

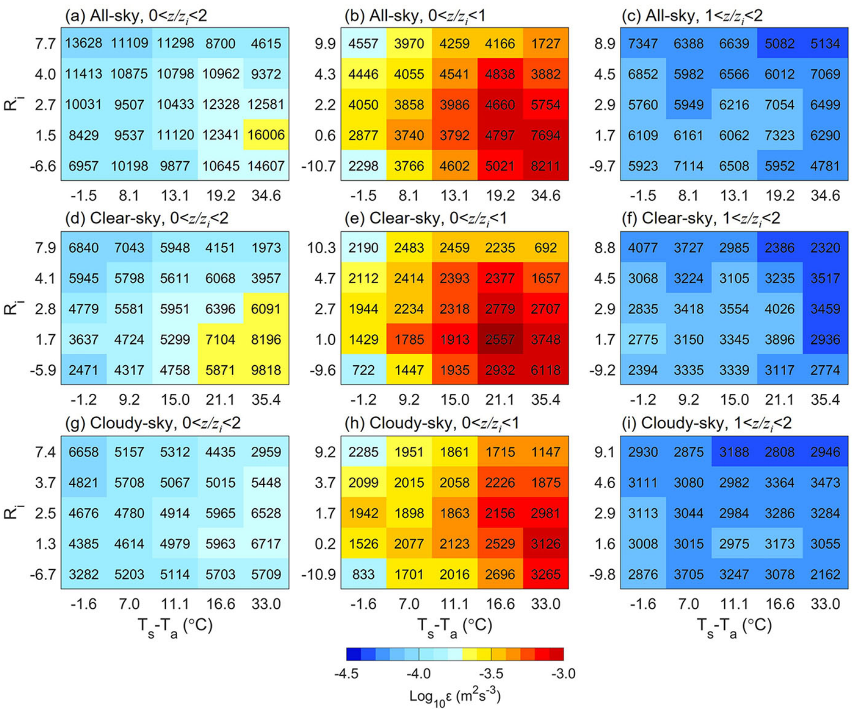

Figure 10. Joint dependence of $Log_{10}\varepsilon$ (color shading) on the gradient Richardson number (Ri) and $T_s - T_a$ in and above the PBL (a, d, g), in the PBL (b, e, h) and above the PBL (c, f, i) over the TP under all-sky (a-c), clear-sky (d-f) and cloudy-sky (g-i) conditions, respectively. The number given in each panel is the total number of samples used.